OPEN

NPG Asia Materials (2017) 9, e351; doi:10.1038/am.2017.5
www.nature.com/am

ORIGINAL ARTICLE

Reliable current changes with selectivity ratio above 10^9 observed in lightly doped zinc oxide films

Un-Bin Han[1], Donghwa Lee[2] and Jang-Sik Lee[1]

Low-power operation of semiconductor devices is crucial for energy conservation. In particular, energy-efficient devices are essential in portable electronic devices to allow for extended use with a limited power supply. However, unnecessary currents always exist in semiconductor devices, even when the device is in its off state. To solve this problem, it is necessary to use switch devices that can turn active devices on and off effectively. For this purpose, high on/off current selectivity with ultra-low off-current and high on-current is required. Here, we report a novel switch behavior with over 10^9 selectivity, a high on-current density of 1 MA cm^{-2}, an ultra-low off-current density of 1 mA cm^{-2}, excellent thermal stability up to 250 °C and abrupt turn-on with 5 mV per decade in solution-processed silver-doped zinc oxide thin films. The selection behavior is attributed to light doping of silver ions in zinc oxide films during electrochemical deposition to generate atomic-scale narrow conduction paths, which can be formed and ruptured at low voltages. Device simulation showed that the new selector devices may be used in ultra-high-density memory devices to provide excellent operation margins and extremely low power consumption.
NPG Asia Materials (2017) **9,** e351; doi:10.1038/am.2017.5; published online 24 February 2017

INTRODUCTION

Recently, emerging non-volatile memory technologies, such as phase-change memory, spin-transfer torque-magnetic memory and resistive switching memory (ReRAM), have been investigated as next-generation technologies to replace conventional flash memory.[1–3] Among them, ReRAM has been extensively studied because of its non-volatile memory characteristics owing to its excellent retention, endurance and high on/off current ratio.[4–7] Furthermore, ReRAM has a simple two-terminal structure, fast switching speed and low power consumption with excellent scalability. ReRAM cells have been integrated into cross-point arrays ($4F^2$) to obtain an area-efficient structure for non-volatile memory applications. In addition to planar cross-point arrays, three-dimensional stackable cross-point arrays have been recently considered to maximize ReRAM density.[8,9]

However, the ReRAM cross-point array has critical problems with sneak current and unnecessary power consumption from neighboring memory cells. In general, ReRAMs are operated by measuring the current difference between a metallic low-resistance state (LRS) and an insulating high-resistance state (HRS). In the cross-point array, however, LRS cells can generate leakage current in neighboring cells. After a sensing current value (HRS current+total leakage currents from other cells) exceeds the LRS current limit, the HRS reading operation fails. Thus, the leakage current from the LRS cells of an ReRAM leads to current sensing failure during the reading of HRS cells.[8] To overcome the leakage current issue, the mixed-ionic-electronic conduction (MIEC) selector was developed by IBM.[10,11] The MIEC is widely accepted as a nearly ideal selector because it shows low off-current (100 pA), high on-current (10 μA) and steep sub-threshold swing characteristics (<60 mV per decade). However, its conduction mechanism is not clearly understood, and its reliability has not yet been confirmed. Tunnel barrier selectors have also been investigated because of their excellent nonlinear *I–V* characteristics.[12] The main mechanisms of the tunnel barrier selectors are direct tunneling (off characteristics) and Fowler–Nordheim tunneling (on characteristics) regarding applied electric fields. It has a very high on-current density (10 MA cm^{-2}) and high selectivity (10^4 ratio). The tunnel barrier device requires a constant electric field, and it degrades the ReRAM writing operation after integration with ReRAM, owing to the resistive states of tunnel barriers. Therefore, to avoid the influence of resistance on selectors, insulator–metal transition (IMT) materials have been investigated with threshold switching characteristics. The representative materials showing IMT characteristics are VO_2, NbO_2 and Ti_4O_7, which exhibit very similar threshold electrical characteristics of high on-current.[13,14] In general, conventional memory devices should be operated stably at or above 85 °C. However, VO_2 cannot be applicable for memory applications because the low transition temperature (~ 65 °C) of VO_2 cannot guarantee the thermal reliability of devices. NbO_2 and Ti_4O_7 are CMOS-compatible materials, and they have been implemented in three-dimensional structures to achieve high density. Both NbO_2 and Ti_4O_7 have been successfully operated with a vertical electrode. Furthermore, NbO_2 has been fully integrated in $4F^2$ 2x-nm technology for one selector-one resistor cross-point

[1]Department of Materials Science and Engineering, Pohang University of Science and Technology (POSTECH), Pohang, Republic of Korea and [2]School of Materials Science and Engineering, Chonnam National University, Gwangju, Korea
Correspondence: Professor J-S Lee, Department of Materials Science and Engineering, Pohang University of Science and Technology (POSTECH), 77 Cheongam-ro, Pohang 790-784, Republic of Korea.
E-mail: jangsik@postech.ac.kr
Received 13 August 2016; revised 16 October 2016; accepted 28 November 2016

arrays.[15,16] However, both NbO_2 and Ti_4O_7 have a high leakage current (sub-μA level), and the transition occurs at approximately 10 μA, thus resulting very poor selectivity for cross-point array applications. The IMT mechanism requires a forming process to obtain the desired behavior. The requirement of high voltage application in the forming process presents a burden regarding the circuit. To avoid the problems of high threshold current in IMT selectors, the ovonic threshold switch, which has sub-100 nA leakage current with excellent on-current characteristics, has been investigated.[17] However, a ReRAM cross-point array still requires much lower leakage current for high-density memory applications. Furthermore, the ovonic threshold switch has a very complicated composition of AsTeGeSiN with a narrow process margin. Additionally, Ag-based threshold switching has been investigated to obtain low leakage current. The co-existence of volatile threshold switching and non-volatile memory switching induced by a conductive Ag filament in a single device has been analyzed.[18] In particular, the threshold switching characteristic is attributed to weak filament formation by a low compliance current. However, this low compliance current limits the operating current of ReRAM. Therefore, to implement a real cross-point array, very low leakage current (<10 pA), sufficient on-current, and simple selector structure are required. In addition, some studies have solved the sneak current issues by adopting new device structures and operation schemes. Self-rectifying resistive switching was introduced for high-density memory applications.[19] Additionally, complementary resistive switching was developed by insertion of very thin active metal layer in resistive switching layers.[20] Both methods have a good potential to be implemented in high-density memory applications, with the advantages of simple device structures and lowered sneak currents. Although diverse efforts have been made to solve the sneak current issue, a novel selector is still required to allow the cross-point array to be used for high-density ReRAM devices.

In this study, we used a light doping of Ag ions in ZnO films as a switching layer by electrochemical deposition (ECD) to develop a novel selector with ultra-low off-current and high on-current. Among various metal oxides, ZnO has been investigated as an attractive material in the field of memory devices because of its low process temperature and large memory window.[21–25] However, pure ZnO films generally have high forming voltages. Therefore, we carried out Ag doping on a ZnO thin film for low-voltage operation of a selector device that does not require an initial forming process, because doping is an effective method to modify the material properties of ZnO thin films.[26] In particular, Ag doping using ECD is the most effective method to control the electrical characteristics of a device with controlled doping concentration. The ECD process can be used to control the doping concentration in ZnO films by adjusting the metal ion concentration, temperature of the solution and applied potential.[27,28] Our study demonstrates that Ag-doped ZnO can be used as a novel selector material of high-density ReRAM by enhancing the metallic filament formation in ZnO thin film.

MATERIALS AND METHODS

Synthesis of 250-nm via-hole patterns on silicon wafers

To fabricate nanoscale selector devices, nanoscale via-hole patterns (with a diameter of 250 nm and a thickness of 100 nm) were fabricated on silicon wafers. First, a 100-nm-thick SiO_2 layer was deposited on a Pt/Ti/SiO_2/Si substrate by plasma-enhanced chemical vapor deposition. Via-hole patterns were formed using KrF lithography followed by reactive-ion etching. The SiO_2 layer was used as the sidewall for device isolation.

Fabrication of 250-nm memory devices

We fabricated Ag-doped ZnO-based nanoscale selector devices by using 250-nm via-hole structures on silicon wafers. A Pt layer was used as the bottom electrode. The Ag-doped ZnO served as the switching layer of the selector devices and was deposited using ECD. The Ag-doped ZnO layer was synthesized using a $Zn(NO_3)_2{\cdot}6H_2O$ aqueous solution with 0, 0.02 and 0.06 mol% $AgNO_3$. The Ag-doped ZnO layer was deposited at −0.5 V and 80 °C. The deposition thickness of Ag-doped ZnO was ~40 nm. A Pt layer with a 100-nm-thick electrode was deposited using an e-beam evaporator and served as the top electrode.

Characterization

A potentiostat/galvanostat (Reference 3000; GAMRY, Warminster, PA, USA) with a three-electrode system was used for ECD and cyclic voltammetry. An ECD of Ag-doped ZnO was performed using galvanostatic polarization. A cyclic voltammogram was measured using potential scanning from open circuit potential (OCP vs Ag/AgCl). The surface morphology and composition of an Ag-doped ZnO-based nanoscale selector device were observed using a scanning electron microscope (FE-SEM; JEM-7401F; JEOL, Akishima, Tokyo, Japan) and a high-resolution transmission electron microscope (HR-(S)TEM-I; JEM 2100F with a Cs corrector on STEM; JEOL). The existence of Ag in the ZnO layer was confirmed using TEM-energy-dispersive X-ray spectroscopy (EDS) and X-ray photoelectron spectroscopy (XPS; ESCA LAB250; VG Scientific, Waltham, MA, USA). Before TEM observations, the samples were prepared using a focused ion beam (FIB; Helios; FEI, Hillsboro, OR, USA). The electrical properties of the selector devices were measured using a semiconductor parameter analyzer (SPA; 4200-SCS, KEITHLEY, Solon, OH, USA). The electrical measurements were performed at various conditions.

First-principle density functional theory (DFT) calculations

DFT calculations were performed with the projector augmented wave method and the generalized gradient approximation of Perdew, Burke and Ernzerhof for the exchange-correlation potential, as implemented in the Vienna Ab-initio Simulation Package (VASP) code.[29,30] The bulk wurtzite ZnO system is composed of 128-atom supercells ($4\times4\times2$ unit cell), and the lattice parameters a and c are obtained as 3.23 and 5.22 Å, respectively, for the primitive unit cell. Monkhorst–Pack k-point sampling with a grid of $2\times2\times2$ was used for the Brillouin zone integration.[31] An energy cutoff of 500 eV was used for the plane-wave representation of the wave functions, and atomic structures were relaxed until all Hellman–Feynman forces were below 0.01 eV $Å^{-1}$. The climbing-image nudged elastic band method with six images was used for locating minimum energy pathways.[32] In the climbing-image nudged elastic band method, the transition state is determined by optimizing a number of intermediate images along the migration path by applying spring force and driving the highest energy image to the saddle point.

RESULTS AND DISCUSSION

We fabricated a selector device with a device size of 250 nm for nanoscale bidirectional switching applications. The device structure is described in Figures 1a and b. SEM results confirmed the Ag-doped ZnO layer in the 250 nm via-hole patterns on the Si substrate (Figure 1c). The thin films were synthesized with uniform thickness. The bottom-up approach using ECD can successfully be employed to fabricate nanoscale threshold switching devices without vacuum deposition systems. The Ag-doped ZnO layer acts as a switching layer for selector applications.

The Ag-doped ZnO layer was deposited by ECD at low temperature. We compared the thin film characteristics of undoped ZnO and Ag-doped ZnO layers, including the cyclic voltammograms of the ZnO, which were measured with various Ag doping concentrations (Supplementary Figure S1a). The electrochemical reduction of the undoped ZnO occurred at −0.75 V, whereas the reduction of the 0.06 mol% Ag-doped ZnO occurred at −0.25 V. The voltage level of the reduction increased with the increased doping concentration

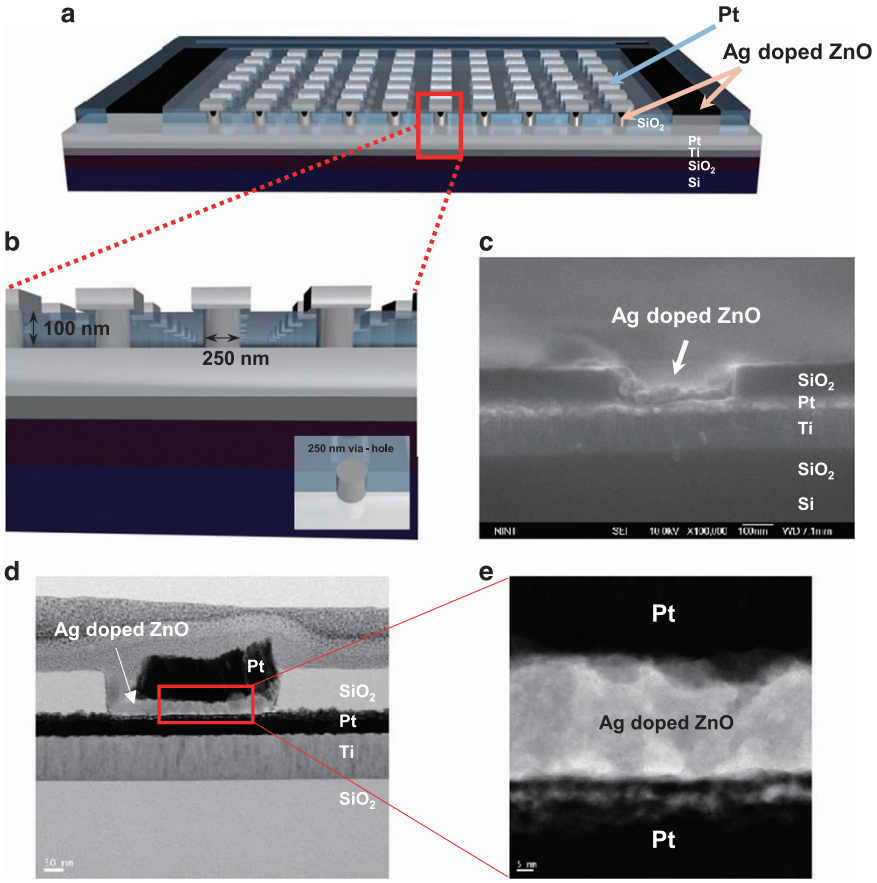

Figure 1 Schematic device structure and microstructure of fabricated nanoscale threshold switching devices. (**a**) Schematic illustration of Ag-doped ZnO-based nanoscale threshold switching devices. (**b**) Cross-sectional schematic view of the device with 250-nm holes patterned on a wafer. (**c**) Cross-sectional SEM image of Ag-doped ZnO-based threshold switching device. (**d**, **e**) Cross-sectional TEM images of Pt/Ag-doped ZnO/Pt device at different magnification levels.

because cations accelerated the electrochemical reduction in the solution. Typical current–time transients of the counter electrode (carbon) and the working electrode (Pt via-hole wafer) during potentiostatic polarization at various doping concentrations are shown in Supplementary Figure S1b. The constant current density produced the uniform thickness of the thin film.

Generally, ZnO thin films are formed by a chemical reaction between Zn^{2+} and OH^- ions in solution, and the thin film formation mechanism is explained by the following equations.[27,33–35]

$$Zn(NO_3)_2 \rightarrow Zn^{2+} + 2NO_3^- \quad (1)$$

$$NO_3^- + H_2O + 2e^- \rightarrow NO_2^- + 2OH^- \quad (2)$$

$$Zn^{2+} + 2OH^- \rightarrow ZnO + H_2O \quad (3)$$

The overall equation is then

$$Zn^{2+} + NO_3^- + 2e^- \rightarrow ZnO + NO_2^- \quad (4)$$

We used TEM to analyze and confirm the surface morphology and composition of the nanoscale 0.06 mol% Ag-doped ZnO layer deposited by ECD. The patterned Pt via-hole substrate and the successful fabrication of the Ag-doped ZnO selector with 40 nm thickness in a 250 nm via-hole were confirmed by TEM (Figure 1d). Figure 1e shows a cross-sectional high-resolution TEM image of the Pt/Ag-doped ZnO/Pt structure. The existence of Ag in the ZnO layer was confirmed by TEM-EDS and XPS (Supplementary Figure S2).

Electrical analysis was performed at various Ag doping concentrations to obtain a volatile Ag filament in the ZnO layer, because the volatile filament property is the most important parameter for selector applications. To observe the effects of Ag doping on the electrical characteristics of the ZnO thin film, $AgNO_3$ with 0, 0.02, 0.06 and 0.1 mol% were injected into the ZnO solution. The undoped ZnO thin film exhibited highly insulating characteristics at low voltage (Supplementary Figure S3a), whereas threshold switching characteristics of the Ag-doped ZnO thin film were observed with increasing Ag concentrations. The 0.02 mol% Ag-doped ZnO films had lower resistivity than those of undoped ZnO, and switching behaviors were observed for both positive and negative polarities (Supplementary Figure S3b). However, the difference between on- and off-current was still low (10^6) for practical applications.

We further investigated 0.06 mol% Ag-doped ZnO to understand how the increased doping concentration affects the switching behavior and current density. Figure 2a shows the current–voltage (*I*–*V*) curves of the bidirectional switching characteristics with a 100-μA compliance current. The as-fabricated device had ultra-low off-current (100 fA), and the current abruptly changed to 100 μA at 0.5 V without an initial forming operation. As the applied bias was swept to negative or

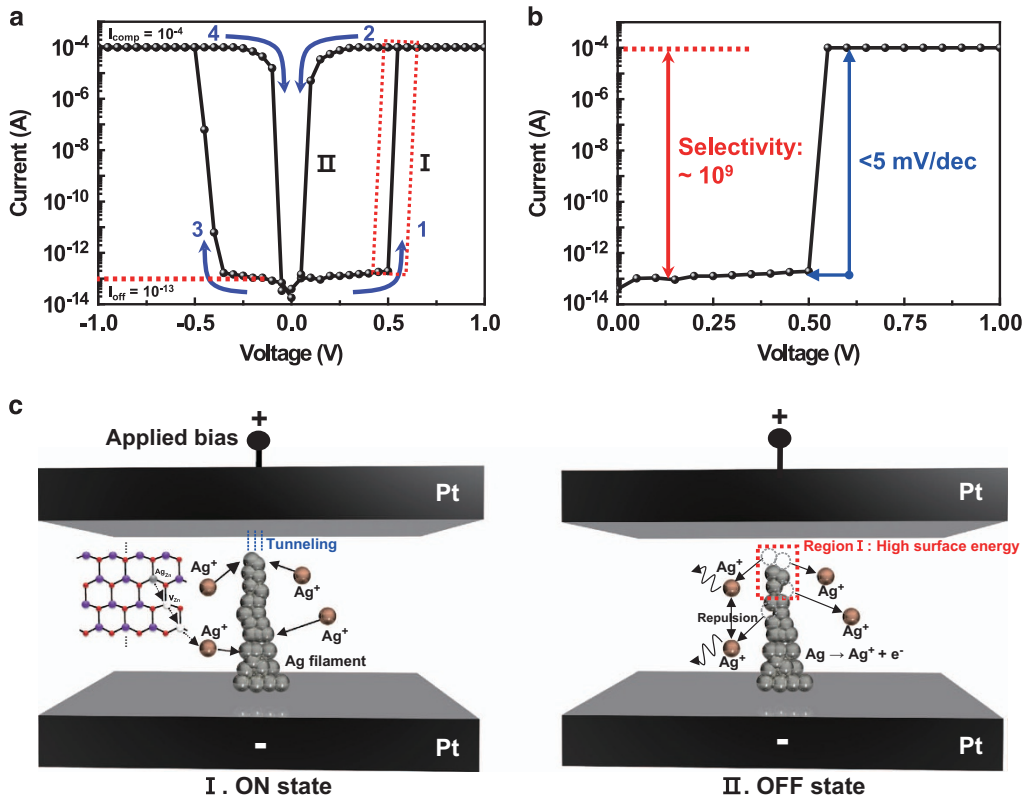

Figure 2 Electrical properties of nanoscale threshold switching devices. (**a**) Electrical characteristics of 0.06 mol% Ag-doped ZnO-based selection device fabricated using ECD. (**b**) Subthreshold slope showing <5 mV per decade for selection device applications. (**c**) Threshold switching mechanism of 0.06 mol % Ag-doped ZnO-based devices.

positive polarity, the device current value was increased from 100 fA to 100 μA at the threshold voltage (V_{Th}). This threshold switching characteristic can be attributed to Ag filament formation in the ZnO layer, and the low operation voltage is explained by the high mobility of Ag ions in the ZnO layer. Further details on the energetics of ionic migration will be discussed in the DFT section. We confirmed a novel selector behavior with a selectivity over 10^9, high on-current density of 1 MA cm^{-2} and extremely abrupt turn-on with 5 mV per decade for the Ag-doped ZnO films, as shown in Figure 2b. The selectivity is defined in the following equation (equation (5)).

$$\text{Selectivity} = (I@V_{On})/(I@V_{Off}) \quad (5)$$

In addition, the effects of film thickness of the 0.06 mol% Ag-doped ZnO thin films on the electrical characteristics of the device were investigated at various deposition times (Supplementary Figure S4). We observed that the switching voltage was decreased with decreased deposition time. In other words, thinner films required lower voltage for current switching. Consequently, the threshold voltage of the selection device could be engineered by controlling the oxide layer thickness through deposition time.

Generally, after a filament is formed in the electrolyte layer, it can maintain its conductivity without applied bias in memory applications. However, the formed filament naturally ruptured in the volatile switch when applied bias was removed. This phenomenon is similar to the threshold switching of IMT operation. The current abruptly decreased at a hold voltage (V_H) of 0.1 V during the backward bias sweep. The threshold switching was also observed at negative polarity (Figure 2a). After the positive sweep, additional filament formation was observed at negative polarity, and the filament was ruptured again at −0.1 V because of its volatile characteristics. This behavior may be applicable to bidirectional two-terminal selectors for integrated cross-point ReRAM devices. The selector characteristics resulted from the Ag doping in the ZnO layer forming a metallic filament. The mechanism of operation of these devices is known as the formation and rupture of a conductive bridge path (e.g., metallic filament) in solid-electrolyte layers.[36–39] Because extrinsic Ag ions have a large diffusion coefficient (i.e., are fast diffusers), Ag ions can easily migrate in the ZnO matrix along the applied electric field.[40,41] After they reached the bottom electrode through the ZnO layer without agglomerating, they formed filaments by combining with electrons at the bottom electrode interface (Figure 2c). The formed filament was very unstable. The Ag ion supplement was limited and thus was insufficient for filament formation. As a result, a narrow gap remained between the formed filament and the electrode. This phenomenon has similarly been observed when devices are scaled down to <40 nm.[42] The limited metal source of electrolytes may be a reason for the gap between the filament and the electrode. In addition, the electric-field has an important effect on filament instability.[38,43,44] In this work, a weak electric field was applied to the electrode. It could not reach the top electrode because low voltage was applied to the 40-nm-thick oxide layer. Thus, tunneling occurred when the contact between the filament and the top electrode was imperfect (e.g., the interface between the filament and the top electrode was in an insulating state). In particular, when the gap between the filament and the top electrode was narrow, this gap was highly affected by the electric field, and the oxide band was bent to allow Fowler–Nordheim tunneling, resulting in high on-current. Accordingly, when the bias was removed, the conductive filament naturally ruptured because it was not sufficiently stable to

retain its conductive state. When bias is removed, the filament of Ag atoms ionizes because of the high surface energy associated with high chemical reactivity around the thin Ag filament.[36,37] Thus, the filament ionized to minimize the surface energy; as a result, the filament ruptured when the applied bias was removed. Therefore, when the radius of the filament is decreased (region I), the instability of surface atoms is accelerated (Gibbs–Thomson effect), the atomic combination of the filament is finally broken, and those atoms are in a free state.[36,45,46] Thus, the highly conductive on-state can be understood on the basis of Ag filament formation, whereas the highly insulating off-state is described by isolated Ag ions in the ZnO layer. In conclusion, the migration of Ag ions plays an important role in the bidirectional threshold switching behavior for selector applications. Experimental verification to show the formation of conductive filaments has been reported.[37,38]

To understand the Ag filament formation in the ZnO layer, first-principle DFT calculations were performed. Because Ag ions are preferentially located in Zn sites, we focused on the energetics of the substitutional $Ag_{Zn}^{'}$ ion in the ZnO layer. Our DFT calculation results showed that the migration barrier of $Ag_{Zn}^{'}$ ion to $V_{Zn}^{''}$ is only 0.19 eV. This result indicates that the $Ag_{Zn}^{'}$ ion can easily migrate to $V_{Zn}^{''}$ in the ZnO if $V_{Zn}^{''}$ exists nearby. In other words, the existence of the nearest neighbor $V_{Zn}^{''}$ can be the bottleneck for the migration process of $Ag_{Zn}^{'}$ ions, and the formation of the $Ag_{Zn}^{'}$–$V_{Zn}^{''}$ complex is the key process determining Ag filament formation. Therefore, this calculation focused on understanding the formation of the $Ag_{Zn}^{'}$–$V_{Zn}^{''}$ complex in the ZnO layer.

Figure 3 shows the relative energetics of two different $Ag_{Zn}^{'}$–$V_{Zn}^{''}$ configurations along the migration pathway. The right side shows the case in which $V_{Zn}^{''}$ sits at the nearest neighbor of $Ag_{Zn}^{'}$ and forms an $Ag_{Zn}^{'}$–$V_{Zn}^{''}$ defect complex (DC) configuration. In contrast, the left-side configuration represents the case in which $Ag_{Zn}^{'}$ and $V_{Zn}^{''}$ are placed separately and act as two isolated defects (ID). We chose the total energy of the ID configuration as a reference state to compare the relative energetic stability of the DC configuration. Our DFT study predicted that an $Ag_{Zn}^{'}$–$V_{Zn}^{''}$ defect complex is less energetically favorable by 0.26 eV than two isolated defects, as shown in the red line of Figure 3a. Hence, the ID configuration is thermodynamically preferred, and spatially separated configuration would prevent the migration of $Ag_{Zn}^{'}$. The repulsive interaction between $Ag_{Zn}^{'}$ and $V_{Zn}^{''}$ can be easily understood on the basis of the negative charge states of both defects. As the charge state of the system decreases, however, the preferred configuration changes. The blue and cyan lines of Figure 3a show the enhanced energetic preference of the DC configuration under electron depletion conditions. For example, the total energy of the DC configuration becomes 0.08 eV lower than the ID configuration under one electron depletion condition, and thus $V_{Zn}^{''}$ migrate into the nearest site of $Ag_{Zn}^{'}$. The energetic preference of the DC configuration increases as the electron deficiency of the system increases. The DC configuration becomes 0.27 eV lower than the ID configuration with two fewer electrons, thus indicating that the complex formation is proportional to the electron deficiency of the system. To understand the relationship between the preferred configuration and electron deficiency, we further studied the variation in electron charge density introduced by the electron depletion, as shown in Figure 3b. The blue isosurfaces represent the regions where the electron density decreased via electron depletion, and the red surfaces represent regions of accumulation. As seen, most of electron density decreased near the $Ag_{Zn}^{'}$ ion under a one-electron depletion condition. This result indicates that the electron depletion neutralized the negative charge state of $Ag_{Zn}^{'}$, and the increased charge state of $Ag_{Zn}^{'}$ weakened the repulsive interaction between $Ag_{Zn}^{'}$ and $V_{Zn}^{''}$. As a result, the formation of the DC configuration becomes thermodynamically favorable. We also investigated the migration barrier of $V_{Zn}^{''}$ to understand the kinetic aspects of $Ag_{Zn}^{'}$–$V_{Zn}^{''}$ complex formation. The migration barrier was obtained by performing climbing-image nudged elastic band calculations.[29,47] Our results indicate that the 0.67 eV migration barrier for $V_{Zn}^{''}$decreased to 0.60 and 0.59 eV under one- and two-electron depletion conditions, respectively. Thus, the migration of $V_{Zn}^{''}$ to form the $Ag_{Zn}^{'}$–$V_{Zn}^{''}$ complex can also be enhanced kinetically under electron depletion conditions. After formation of the $Ag_{Zn}^{'}$–$V_{Zn}^{''}$ complex, the $Ag_{Zn}^{'}$ ion can easily migrate into the $V_{Zn}^{''}$ site. Under forward bias, Ag ions migrate to the negatively charged bottom electrode through the $V_{Zn}^{''}$ site and form an Ag filament along the direction of the external bias, as shown in Figure 2c. Thus, the formation of $Ag_{Zn}^{'}$–$V_{Zn}^{''}$ complex facilitates the formation of the Ag filament in the ZnO layer. In conclusion, the Ag filament formation in the ZnO layer under forward bias is a result of the formation of $Ag_{Zn}^{'}$–$V_{Zn}^{''}$ complex induced by electron deficiency in the ZnO layer. The low migration barrier of the

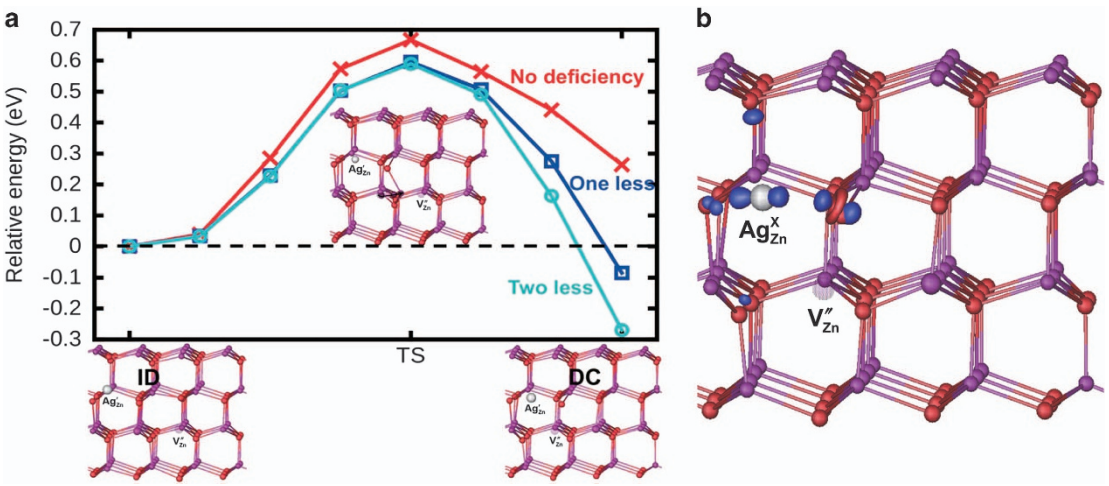

Figure 3 First-principle DFT calculations for behaviors of substitutional $Ag_{Zn}^{'}$ ion in the ZnO layer. (**a**) Relative energetics of two different $Ag_{Zn}^{'}$–$V_{Zn}^{''}$ configurations along the migration pathway. (**b**) Variation in electron charge density introduced by electron depletion (blue: regions where the electron density has decreased by electron depletion, red: regions of accumulation).

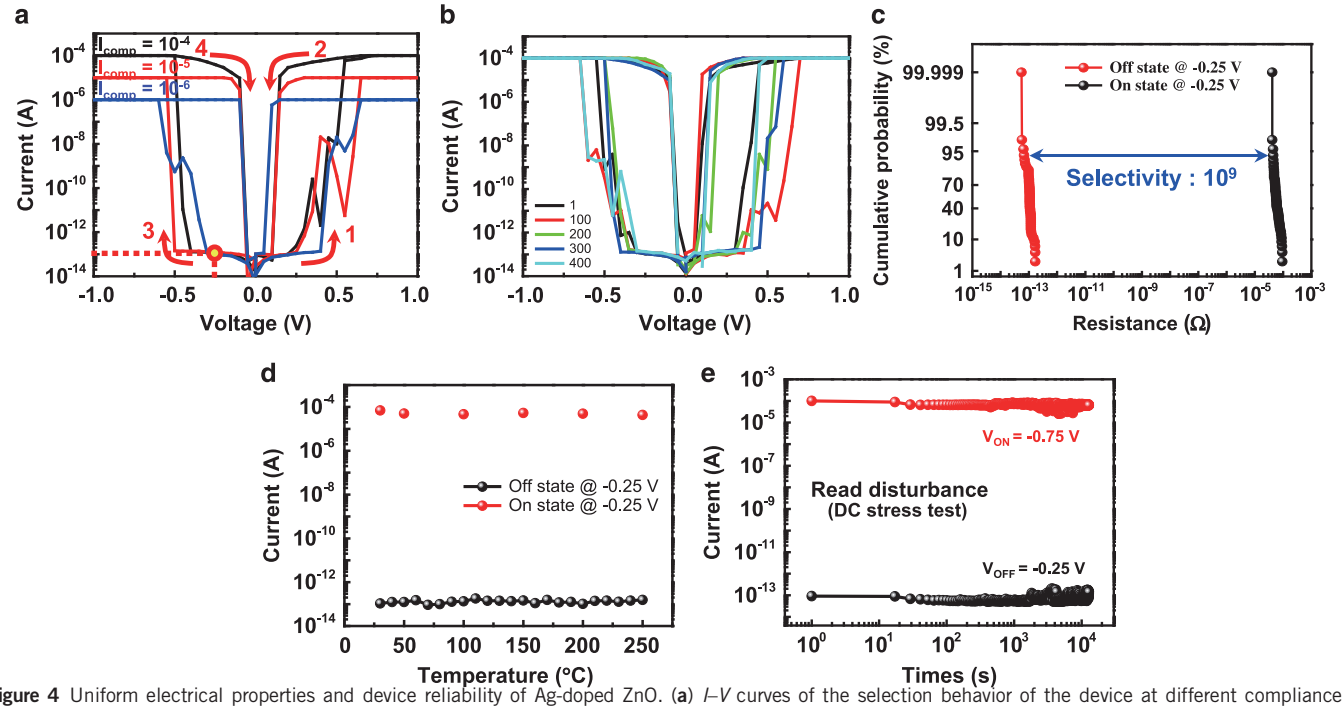

Figure 4 Uniform electrical properties and device reliability of Ag-doped ZnO. (**a**) *I–V* curves of the selection behavior of the device at different compliance currents. (**b**) Reliable device operation up to 400 DC cycles. (**c**) Cumulative probability of on- and off-states measured at −0.25 V. (**d**) Thermal stability measured at various temperatures. (**e**) DC stress test measured at −0.25 and −0.75 V, which are equivalent to OFF- and ON-state, respectively.

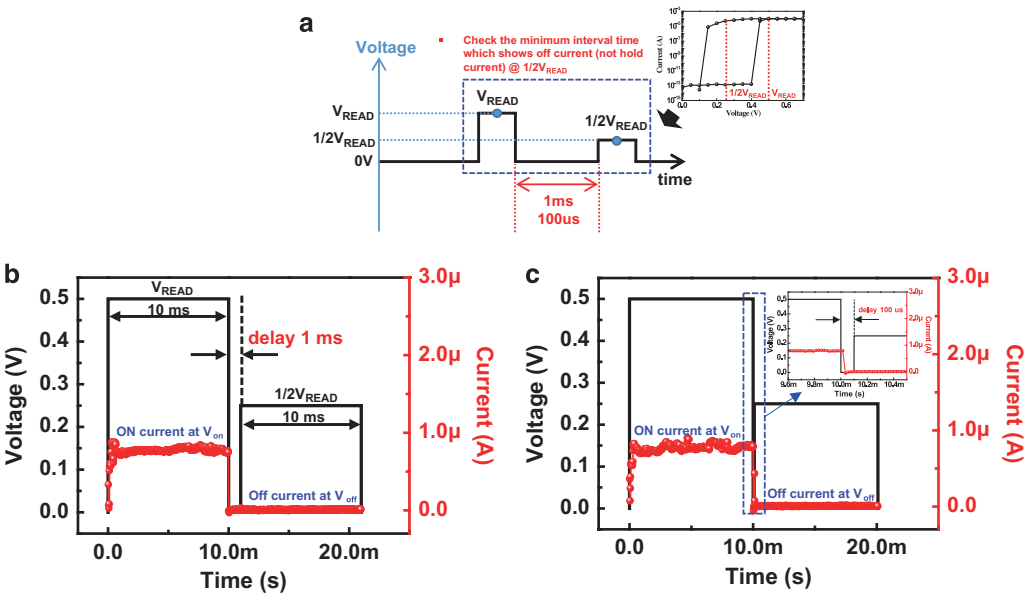

Figure 5 AC measurement of Ag-doped ZnO selection devices. (**a**) Measurement scheme for real-time observation of filament rupture. Delay time of (**b**) 1 ms and (**c**) 100 μs.

Ag'_{Zn} ions contributes to the ultra-fast growth of the conductive path at low voltage in the ZnO layer. Therefore, the migration of Ag ions through the V''_{Zn} site is a key process in the formation of a metallic filament in the ZnO layer, and the Ag filament can be sequentially formed at low voltage (<0.5 V).

Protons can be incorporated in the ZnO layer during ECD. It has been reported that the switching properties of filamentary devices is affected by H^+ and OH^- ions.[48–50] Filament formation is reportedly accelerated by H^+ and OH^- ions, and this effect increases off-current. In our study, however, the device showed low off-current (~100 fA); we performed a comparative study of the electrical properties of the ZnO layer according to the doping concentrations in the ZnO layer (Supplementary Figure S3). For the undoped ZnO case, only very low current was measured. However, after doping with a small amount of Ag, current changes from pA to mA were reliably obtained. Therefore, the highly selective behavior was obtained because of Ag in the ZnO layer. Moisture can strongly affect the electrical properties. However, in this case, the ZnO layer was fully passivated by sidewalls and top

electrodes; consequently, we believe the effect of moisture on electrical properties of Ag-doped ZnO devices in this study is minimal. In addition, no changes in electrical properties according to the time and/or number of operation cycles were observed (Figure 4). Additional experiments were carried out in both air and vacuum to examine the effects of moisture (Supplementary Figure S5). To measure and compare the influence of ambient atmosphere, the samples were held in air and vacuum for 2 h. There was almost no change in current levels and switching voltages in either air or vacuum.

Our 0.1 mol% Ag-doped ZnO-based devices showed ReRAM characteristics. By increasing the Ag-doping concentration in the ZnO layer, a thicker filament than that of 0.06 mol% Ag-doped ZnO was formed. This thick filament could not be ruptured by itself, and application of a negative bias was necessary to rupture the filament. Therefore, the filament was ruptured by Joule heating of the high current flow at negative bias and in the presence of the electric field (Supplementary Figure S3c). The threshold characteristics of a 0.06 mol% Ag-doped ZnO-based device with volatile behavior were observed in various compliance current levels from 1 to 100 μA (Figure 4a). Figure 4b shows the DC *I*–*V* curves of 400 DC cycles. There was no noticeable degradation of the device beyond 400 cycles. In addition, we confirmed reliable on- and off-states with a high selectivity of 10^9 (Figure 4c). To evaluate stability at high temperature, the device was measured at temperatures up to 250 °C and showed no noticeable degradation (Figure 4d). Furthermore, constant voltage stress was applied to the device to confirm the excellent immunity of the read disturbance (Figure 4e). We confirmed that the 0.06 mol% Ag-doped ZnO layer had good electrical characteristics for selection devices through various electrical analyses.

We measured the selector behavior in the AC mode. We applied 10 ms of read voltage (V_{Read}) and half-read voltage ($½V_{Read}$), which corresponded to on- and off-bias of the selector, to confirm on- and off-states, as shown in Figure 5a. To confirm the off-state in the AC mode, delay time was inserted before $½V_{Read}$. We assessed the current values at $½V_{Read}$ after applying V_{Read}; the device exhibited clear off-current values at delay times of 1 ms and 100 μs without any degradation (Figures 5b and c). In addition to 100 μs delay time, we measured the device at delay times of 1 μs and 100 ns. The device was successfully changed to the off-state. (Supplementary Figure S6). Furthermore, we assessed the switching time of the selector. We applied a 100-ns-wide pulse to the device. As shown in Supplementary Figure S7, the selector was successfully operated at this pulse width. This finding confirms that the selector device can be operated stably in the AC mode.

In this study, we further evaluated cross-point array feasibility by *I*–*V* fitting of selectors and resistors using MATLAB and HSPICE simulation tools.[51,52] The simulated one selector-one resistor results showed an excellent readout margin (almost 98% in a 16-Mb array) and low HRS reading power consumption (100 nW at 16-Mb density) that is suitable for terabit-density devices. Finally, it will be very important to implement this selection device in one selector-one resistor device integration for possible application to high-density cross-point memory devices. One selector-one resistor device fabrication and characterization will be performed on the basis of this work in the near future.

In conclusion, we report a novel selection behavior observed in Ag-doped ZnO thin films. The selection behavior was controlled by the concentration of Ag ions in ZnO thin film during growth. It was found that the concentration of Ag ions determines off-current level and filament formation characteristics of the devices. To obtain a reliable and reproducible volatile filament formation/rupture and low off-current, the concentration of Ag ions was carefully controlled during the ECD process. The Ag ions in the ZnO layer formed a highly conductive filament through application of an externally applied bias, and this filament was naturally ruptured when the applied bias was removed. The device exhibited high selectivity (10^9), uniform switching characteristics, ultra-low off-current density and electrical reliability. Furthermore, stable operation up to 250 °C without any noticeable degradation was demonstrated. Most significantly, the device was able to be turned on and off with a slope of 5 mV per decade.

CONFLICT OF INTEREST

The authors declare no conflict of interest.

ACKNOWLEDGEMENTS

This work was supported by the National Research Foundation of Korea (NRF-2016M3D1A1027663 and NRF-2015R1A2A1A15055918). This work was also supported by the Future Semiconductor Device Technology Development Program (10045226) funded by the Ministry of Trade, Industry & Energy (MOTIE)/Korea Semiconductor Research Consortium (KSRC). Computational work was supported by Chonnam National University, 2015 and the Korea Institute of Science and Technology Information with supercomputing resources, including technical support, No. KSC-2015-C3-034. In addition, this work was partially supported by the Brain Korea 21 PLUS project (Center for Creative Industrial Materials).

1 Onofrio, N., Guzman, D. & Strachan, A. Atomic origin of ultrafast resistance switching in nanoscale electrometallization cells. *Nat. Mater.* **14**, 440–446 (2015).
2 Kent, A. D. & Worledge, D. C. A new spin on magnetic memories. *Nat. Nanotechnol.* **10**, 187–191 (2015).
3 Chen, J. Y., Huang, C. W., Chiu, C. H., Huang, Y. T. & Wu, W. W. Switching kinetic of VCM-based memristor: evolution and positioning of nanofilament. *Adv. Mater.* **27**, 5028–5033 (2015).
4 Han, U.-B. & Lee, J.-S. Integration scheme of nanoscale resistive switching memory using bottom-up processes at room temperature for high-density memory applications. *Sci. Rep.* **6**, 28966 (2016).
5 Gu, C. & Lee, J.-S. Flexible hybrid organic-inorganic perovskite memory. *ACS Nano* **10**, 5413–5418 (2016).
6 Pan, F., Gao, S., Chen, C., Song, C. & Zeng, F. Recent progress in resistive random access memories: materials, switching mechanisms, and performance. *Mater. Sci. Eng. R* **83**, 1–59 (2014).
7 Valov, I., Waser, R., Jameson, J. R. & Kozicki, M. N. Electrochemical metallization memories—fundamentals, applications, prospects. *Nanotechnology* **22**, 289502 (2011).
8 Seok, J. Y., Song, S. J., Yoon, J. H., Yoon, K. J., Park, T. H., Kwon, D. E., Lim, H., Kim, G. H., Jeong, D. S. & Hwang, C. S. A review of three-dimensional resistive switching cross-bar array memories from the integration and materials property points of view. *Adv. Funct. Mater.* **24**, 5316–5339 (2014).
9 Lee, W., Park, J., Kim, S., Woo, J., Shin, J., Choi, G., Park, S., Lee, D., Cha, E., Lee, B. H. & Hwang, H. High current density and nonlinearity combination of selection device based on $TaO_x/TiO_2/TaO_x$ structure for one selector-one resistor arrays. *ACS Nano* **6**, 8166–8172 (2012).
10 Saranya, A. M., Pla, D., Morata, A., Cavallaro, A., Canales-Vázquez, J., Kilner, J. A., Burriel, M. & Tarancón, A. Engineering mixed ionic electronic conduction in $La_{0.8}Sr_{0.2}MnO_{3+\delta}$ nanostructures through fast grain boundary oxygen diffusivity. *Adv. Energy Mater.* **5**, 7448–7460 (2015).
11 Messerschmitt, F., Kubicek, M., Schweiger, S. & Rupp, J. L. M. Memristor kinetics and diffusion characteristics for mixed anionic-electronic $SrTiO_{3-\delta}$ bits: the memristor-based Cottrell analysis connecting material to device performance. *Adv. Funct. Mater.* **24**, 7448–7460 (2014).
12 Wang, M., Zhou, J., Yang, Y., Gaba, S., Liu, M. & Lu, W. D. Conduction mechanism of a TaO_x-based selector and its application in crossbar memory arrays. *Nanoscale* **7**, 4964–4970 (2015).
13 O'Callahan, B. T., Jones, A. C., Hyung Park, J., Cobden, D. H., Atkin, J. M. & Raschke, M. B. Inhomogeneity of the ultrafast insulator-to-metal transition dynamics of VO_2. *Nat. Commun.* **6**, 6849 (2015).
14 Lee, S., Woo, J., Lee, D., Cha, E., Park, J., Moon, K., Song, J., Koo, Y. & Hwang, H. Tunnel barrier engineering of titanium oxide for high non-linearity of selector-less resistive random access memory. *Appl. Phys. Lett.* **104**, 052108 (2014).
15 Kim, S. G., Ha, T. J., Kim, S., Lee, J. Y., Kim, K. W., Shin, J. H., Park, Y. T., Song, S. P., Kim, B. Y., Kim, W. G., Lee, J. C., Lee, H. S., Song, J. H., Hwang, E. R., Cho, S. H., Ku, J. C., Kim, J. I., Kim, K. S., Yoo, J. H., Kim, H. J., Jung, H. G.,

Lee, K. J., Chung, S., Kang, J. H., Lee, J. H., Kim, H. S., Hong, S. J., Gibson, G. & Jeon, Y. Improvement of characteristics of NbO_2 selector and full integration of $4F^2$ 2x-nm tech 1S1R ReRAM. in *IEEE Int. Electron Devices Meeting (IEDM) 2015*, 10.3.1–10.3.4 (IEEE, 2015).
16 Kim, W. G., Lee, H. M., Kim, B. Y., Jung, K. H., Seong, T. G., Kim, S., Jung, H. C., Kim, H. J., Yoo, J. H. & Lee, H. D. in *2014 Symp. on VLSI Technology (VLSI-Technology): Digest of Technical Papers* 1–2 (IEEE, 2014).
17 Manivannan, A., Myana, S. K., Miriyala, K., Sahu, S. & Ramadurai, R. Low power ovonic threshold switching characteristics of thin $GeTe_6$ films using conductive atomic force microscopy. *Appl. Phys. Lett.* **105**, 243501 (2014).
18 Sun, H., Liu, Q., Li, C., Long, S., Lv, H., Bi, C., Huo, Z., Li, L. & Liu, M. Direct observation of conversion between threshold switching and memory switching induced by conductive filament morphology. *Adv. Funct. Mater.* **24**, 5679–5686 (2014).
19 Gao, S., Zeng, F., Li, F., Wang, M., Mao, H., Wang, G., Song, C. & Pan, F. Forming-free and self-rectifying resistive switching of the simple Pt/TaO_x/n-Si structure for access device-free high-density memory application. *Nanoscale* **7**, 6031–6038 (2015).
20 Gao, S., Zeng, F., Wang, M., Wang, G., Song, C. & Pan, F. Tuning the switching behavior of binary oxide-based resistive memory devices by inserting an ultra-thin chemically active metal nanolayer: a case study on the Ta_2O_5-Ta system. *Phys. Chem. Chem. Phys.* **17**, 12849–12856 (2015).
21 Xu, D. L., Xiong, Y., Tang, M. H., Zeng, B. W. & Xiao, Y. G. Bipolar and unipolar resistive switching modes in $Pt/Zn_{0.99}Zr_{0.01}O/Pt$ structure for multi-bit resistance random access memory. *Appl. Phys. Lett.* **104**, 183501 (2014).
22 Xu, D., Xiong, Y., Tang, M. & Zeng, B. Coexistence of the bipolar and unipolar resistive switching behaviors in vanadium doped ZnO films. *J. Alloys Compd.* **584**, 269–272 (2014).
23 Tang, M. H., Jiang, B., Xiao, Y. G., Zeng, Z. Q., Wang, Z. P., Li, J. C. & He, J. Top electrode-dependent resistance switching behaviors of ZnO thin films deposited on $Pt/Ti/SiO_2$/Si substrate. *Microelectron. Eng.* **93**, 35–38 (2012).
24 Qi, J., Olmedo, M., Ren, J. J., Zhan, N., Zhao, J. Z., Zheng, J. G. & Liu, J. L. Resistive switching in single epitaxial ZnO nanoislands. *ACS Nano* **6**, 1051–1058 (2012).
25 Liu, Z-J, Gan, J-Y & Yew, T-R ZnO-based one diode-one resistor device structure for crossbar memory applications. *Appl. Phys. Lett.* **100**, 153503 (2012).
26 Li, Y., Zhao, X. & Fan, W. Structural, electronic, and optical properties of Ag-doped ZnO nanowires: first principles study. *J. Phys. Chem. C* **115**, 3552–3557 (2011).
27 Thomas, M. A., Sun, W. W. & Cui, J. B. Mechanism of Ag doping in ZnO nanowires by electrodeposition: experimental and theoretical insights. *J. Phys. Chem. C* **116**, 6383–6391 (2012).
28 Thomas, M. A. & Cui, J. B. Electrochemical route to p-type doping of ZnO nanowires. *J. Phys. Chem. Lett.* **1**, 1090–1094 (2010).
29 Perdew, J. P., Burke, K. & Ernzerhof, M. Generalized gradient approximation made simple. *Phys. Rev. Lett.* **77**, 3865–3868 (1996).
30 Blöchl, P. E. Projector augmented-wave method. *Phys. Rev. B* **50**, 17953–17979 (1994).
31 Monkhorst, H. J. & Pack, J. D. Special points for Brillouin-zone integrations. *Phys. Rev. B* **13**, 5188–5192 (1976).
32 Henkelman, G., Uberuaga, B. P. & Jónsson, H. A climbing image nudged elastic band method for finding saddle points and minimum energy paths. *J. Chem. Phys.* **113**, 9901–9904 (2000).
33 Dai, S., Li, Y., Du, Z. & Carter, K. R. Electrochemical deposition of ZnO hierarchical nanostructures from hydrogel coated electrodes. *J. Electrochem. Soc.* **160**, D156–D162 (2013).
34 Sun, S., Jiao, S., Zhang, K., Wang, D., Gao, S., Li, H., Wang, J., Yu, Q., Guo, F. & Zhao, L. Nucleation effect and growth mechanism of ZnO nanostructures by electrodeposition from aqueous zinc nitrate baths. *J. Cryst. Growth* **359**, 15–19 (2012).
35 Illy, B. N., Cruickshank, A. C., Schumann, S., Da Campo, R., Jones, T. S., Heutz, S., McLachlan, M. A., McComb, D. W., Riley, D. J. & Ryan, M. P. Electrodeposition of ZnO layers for photovoltaic applications: controlling film thickness and orientation. *J. Mater. Chem.* **21**, 12949 (2011).
36 La Barbera, S., Vuillaume, D. & Alibart, F. Filamentary switching: synaptic plasticity through device volatility. *ACS Nano* **9**, 941–949 (2015).
37 van den Hurk, J., Linn, E., Zhang, H., Waser, R. & Valov, I. Volatile resistance states in electrochemical metallization cells enabling non-destructive readout of complementary resistive switches. *Nanotechnology* **25**, 425202 (2014).
38 Hino, T., Hasegawa, T., Tanaka, H., Tsuruoka, T., Terabe, K., Ogawa, T. & Aono, M. Volatile and nonvolatile selective switching of a photo-assisted initialized atomic switch. *Nanotechnology* **24**, 384006 (2013).
39 Hasegawa, T., Terabe, K., Tsuruoka, T. & Aono, M. Atomic switch: atom/ion movement controlled devices for beyond von-neumann computers. *Adv. Mater.* **24**, 252–267 (2012).
40 Xue, W. H., Xiao, W., Shang, J., Chen, X. X., Zhu, X. J., Pan, L., Tan, H. W., Zhang, W. B., Ji, Z. H., Liu, G., Xu, X. H., Ding, J. & Li, R. W. Intrinsic and interfacial effect of electrode metals on the resistive switching behaviors of zinc oxide films. *Nanotechnology* **25**, 425204 (2014).
41 Huang, G. Y., Wang, C. Y. & Wang, J. T. First-principles study of diffusion of Li, Na, K and Ag in ZnO. *J. Phys. Condens. Matter* **21**, 345802 (2009).
42 Yang, Y., Gao, P., Li, L., Pan, X., Tappertzhofen, S., Choi, S., Waser, R., Valov, I. & Lu, W. D. Electrochemical dynamics of nanoscale metallic inclusions in dielectrics. *Nat. Commun.* **5**, 4232 (2014).
43 Wang, H., Du, Y., Li, Y., Zhu, B., Leow, W. R., Li, Y., Pan, J., Wu, T. & Chen, X. Configurable resistive switching between memory and threshold characteristics for protein-based devices. *Adv. Funct. Mater.* **25**, 3825–3831 (2015).
44 Karpov, V. G., Kryukov, Y. A., Savransky, S. D. & Karpov, I. V. Nucleation switching in phase change memory. *Appl. Phys. Lett.* **90**, 123504 (2007).
45 Tappertzhofen, S., Linn, E., Bottger, U., Waser, R. & Valov, I. Nanobattery effect in RRAMs-implications on device stability and endurance. *IEEE Electron. Dev. Lett.* **35**, 208–210 (2014).
46 Valov, I., Linn, E., Tappertzhofen, S., Schmelzer, S., van den Hurk, J., Lentz, F. & Waser, R. Nanobatteries in redox-based resistive switches require extension of memristor theory. *Nat. Commun.* **4**, 1771 (2013).
47 Kresse, G. & Furthmuller, J. Efficiency of ab-initio total energy calculations for metals and semiconductors using a plane-wave basis set. *Comput. Mater. Sci.* **6**, 15–50 (1996).
48 Tappertzhofen, S., Valov, I., Tsuruoka, T., Hasegawa, T., Waser, R. & Aono, M. Generic relevance of counter charges for cation-based nanoscale resistive switching memories. *ACS Nano* **7**, 6396–6402 (2013).
49 Tsuruoka, T., Terabe, K., Hasegawa, T., Valov, I., Waser, R. & Aono, M. Effects of moisture on the switching characteristics of oxide-based, bapless-type atomic switches. *Adv. Funct. Mater.* **22**, 70–77 (2012).
50 Kim, S., Lee, D., Park, J., Jung, S., Lee, W., Shin, J., Woo, J., Choi, G. & Hwang, H. Defect engineering: reduction effect of hydrogen atom impurities in HfO_2-based resistive-switching memory devices. *Nanotechnology* **23**, 325702 (2012).
51 Lee, D., Park, J., Park, S., Woo, J., Moon, K., Cha, E., Lee, S., Song, J., Koo, Y. & Hwang, H. in *IEEE Int. Electron Devices Meeting (IEDM) 2013*, 10.7.1–10.7.4 (IEEE, 2013).
52 Cha, E., Woo, J., Lee, D., Lee, S., Song, J., Koo, Y., Lee, J., Park, C. G., Yang, M. Y., Kamiya, K., Shiraishi, K., Magyari-Kope, B., Nishi, Y. & Hwang, H. in *IEEE Int. Electron Devices Meeting (IEDM) 2013,* 10.5.1–10.5.4 (IEEE, 2013).

Supplementary Information accompanies the paper on the NPG Asia Materials website (http://www.nature.com/am)